Effect of the Pumping-injection flow rate on Heat Transfer Characteristic of Borehole Heat Exchangers for Coupling Ground-Source Heat Pump System

Jiuchen Ma [1,2] , Qian Jiang [1,2,*] , QuLi Zhang [1,2] , Yacheng Xie [1,2] , Yahui Wang [1,2] , Feiyu Yi [1,2]

* Correspondence: 596797782@qq.com [1] School of Energy Safety Engineering, Tianjin Chengjian University, Tianjin 300384, China.
Full list of author information is available at the end of the article

Abstract: A coupling ground source heat pump system (CGSHP) is established in areas where groundwater is shallow but the seepage velocity is weak, which sets up pumping and injection wells on both sides of borehole heat exchangers (BHEs). A convection-dispersion analytical model of excess temperature in aquifer that considers groundwater forced seepage and axial effects and thermal dispersion effects is proposed. A controllable forced seepage sandbox is built by equation analysis method and similarity criteria. Through indoor test and the proposed analytical model, the correctness and accuracy of the numerical simulation software FEFLOW7.1 is verified. The influence of different pumping-injection flow rate on the heat transfer characteristic of BHEs is studied by numerical simulation. The results show that the average heat efficiency coefficient of BHEs increases and the heat influence range of downstream BHEs expands with the increasing of pumping-injection flow rate. The relation curve between *Pe* and the increment of heat transfer rate per unit depth of BHEs ($\Delta\ \overline{q}$) is distributed as Gaussian function. The pumping-injection flow rate that makes Darcy velocity reaches 0.6×10^{-6}~1.4×10^{-6} $m\cdot s^{-1}$ in the aquifer is the best reference range for CGSHP system，so 400~600 $m^3\cdot d^{-1}$ is taken as the best pumping-injection flow rate in this paper.

Keywords: coupling ground source heat pump system; groundwater forced seepage; heat transfer; laboratory experiment; numerical simulation; analytical model

1. Introduction

Shallow geothermal resources in China are abundant but uneven. The relevant documents clearly point out that the development and utilization of shallow geothermal energy should follow the principle of adaption to local conditions (National Development and Reform Commission 2017; China Geological Survey 2018). Ground source heat pump (GSHP) system, as one of the main techniques of shallow geothermal production (Richard 2014; Richard and Marvin 2011), should take full account of local conditions in the application process. Moreover, borehole heat exchangers (BHEs) constitute a core part of the technology and the magnitude of its heat exchange quantity directly affects the efficiency of the overall unit. Therefore, it is particularly important to enhance heat transfer around BHEs.

The heat transfer performance of BHEs is studied usually by four methods, i.e., analytical method, numerical method, and in-situ thermal response test (TRT) and laboratory test. In most related fields, one or two of the above methods are adopted commonly to study the effect of natural groundwater seepage on the heat transfer performance of BHEs (Angelotti and Alberti 2014; Jinzhong 2017; Choi and Park 2013; Huajun and Chengying 2009).

Numerical simulations give accurate solutions that are conducive to theoretical analysis but need extensive computational time. Hence, numerous numerical simulation softwares are often applied to the research and design of BHEs, but the correctness and accuracy of these

softwares should be verified before (Alessandro and Rajandrea 2014; Yanling and Xiaoli 2017). Angelotti et al. (Angelotti and Alberti 2014) explore the influence of groundwater seepage velocity on the heat transfer characteristics of rock and soil layer by establishing a single U-pipe heat transfer model through the codes MODFLOW/MT3DMS. Meanwhile, the solution of numerical model is validated through the analytical solution of moving line source model (MLS) on the premise that the U-pipe is simplified into an infinite line source. Hecht et al. (Jozsef and Michael 2013) use FEFLOW, a finite element numerical simulation software, to perform the transient heat transport simulations for the fifteen scenarios of 25 boreholes and study the distribution of hydrodynamic field and temperature field in the homogeneous confined aquifer. Li et al. (Chaofeng and Peter 2018) analyze the effect of unsaturated soil properties and groundwater flow on the performance of GSHP system by the simulation software COMSOL Multiphysics. The numerical model is validated by combining experimental test results with the analytical model that takes the multiple-layer substrates and groundwater flow into consideration.

Analytical models are preferred in most practical applications because of their excellent computational time and flexibility for parameterized design. The method of moving heat-source is applied in most analytical models to solve the problem of heat transfer under the impact of groundwater seepage (Min and Alvin 2015). Sutton et al. (Matthew and Darin 2003) and Diao et al. (Nairen and Qinyun 2004) present an analytical model considering groundwater flow. They both concluded that groundwater flow could change considerably the temperature distribution in the vicinity of the boreholes. Molina-Giraldo et al. (Nelson and Peter 2011) evaluate the influence of thermal dispersion on temperature plumes of geothermal systems by using analytical models. In the above analytical models, the axial effect is not considered and the borehole is considered to be a moving infinite line heat source. Molina-Giraldo et al. (Nelson and Philipp 2011) propose a moving finite line source model (MFLS) which considers the combined effect of groundwater flow and axial effects but does not take the influence of thermal dispersion into account. Groundwater seepage affects heat transfer by involving gross heat convection and thermal dispersion, which is significant for the long-term temperature response of BHEs (Luo and Rohn 2016). Therefore, an optimized analytical model, which considers the thermal dispersion effect in the MFLS model, is proposed in this paper.

TRTs are applied to some real environments that can truly reflect the heat transfer process of BHEs under the specific regional climatic characteristics and hydrogeological conditions. Most TRTs are performed on a test borehole to estimate the thermo-physical properties and borehole thermal resistance (Huajun and Chengying 2009; Jin and Joachim 2013; Wonjun and Ryozo 2015). From the viewpoint of model validation, the data from TRTs is not suitable because TRTs' test times are short (usually 48-72 hours) and are susceptible to uncontrollable factors such as weather conditions during testing (Min and Alvin 2015; David and Elmore 2018; Ali and Michel 2014). The indoor sandbox experiments enable to change some parameters, which is conducive to improve the speed and test accuracy of the experiment (Guozhu and Yimu 2016; Linlin and Lei 2015) because the experimental requirements have well controllability comparing with the TRT.

Most studies (Erol and François 2018; Martin and Jonathan 2018; Junye and Gui 2017; Wenke and Hongxing 2014) point out that the presence of groundwater significantly affects the heat transfer between BHE and its surrounding aquifer. However, most of these study conclusions are obtained under the condition of high natural seepage velocity, which is generally higher than 10^{-8} m·s^{-1}. However, many areas such as the Bohai Rim plain have abundant groundwater reserves but the natural seepage velocity there is generally lower than 10^{-8} m·s^{-1}. In this case, it is usually considered that groundwater seepage has almost no effect on heat transfer of BHEs. At this time, using the traditional GSHP system would render groundwater idle without having the positive effect that it should have. Therefore, it is necessary to optimize the traditional GSHP system for this special hydrogeological condition.

For the long-term application of GSHP system, the cold and heat accumulation around BHEs and the heat transfer quantity of BHEs decay year-by-year, domestic and foreign scholars have proposed some optimized methods and improved measures to regulate heat balance of the soil. Such as, solar assisted GSHP system (Østergaard and Duic 2019; Nouri and Noorollahi 2019; Biglarian and Saidi 2019), and cooling tower assisted GSHP system (Liu and Li 2018; Gong and Xia 2018). Giti Nouri et al. (Nouri and Noorollahi 2019) and Zhijian Liu et al. (Liu and Li 2018) study solar assisted GSHP system and cooling tower assisted GSHP system, respectively. Their research results show that the application of these hybrid systems could be helpful to reach considerable savings of energy through using free resources of stored heat in the ground and sun or air. However, solar-assisted GSHP system and cooling tower assisted GSHP system occupy a large land area and are greatly affected by seasonal and environmental factors.

Thus, this paper proposes a coupling ground source heat pump (CGSHP) system which sets up pumping and injection wells on both sides of BHEs' well group by basing on GSHP system in Tianjin, China and combining with the local special hydrogeological conditions. According to CGSHP system proposed in this paper, a laboratory experiment system is established and a convection-dispersion analytical model of excess temperature that considers groundwater forced seepage and axial effects and thermal dispersion effects is proposed. The correctness and accuracy of the numerical simulation software FEFLOW7.1 is validated with the laboratory sandbox test and the proposed convection-dispersion analytical model. Meanwhile, the purpose of this paper is to study the enhancement effect of heat transfer of BHEs and reveal the evolution law of the temperature field and hydrodynamic field of the aquifer under different pumping-injection flow rate by the numerical simulation.

2. Geological survey and underground thermo-physical properties

2.1. Geological survey

China's Bohai Rim region includes the plains of the four provinces of Liaoning, Hebei, Tianjin, Shandong and the surrounding mountainous areas (including the two peninsulas). The Bohai Rim plain is formed in the middle Pleistocene (Q2) and the late Pleistocene (Q3) to the Holocene (Q4) in the Quaternary period. The final formation of the Bohai Rim region is the result of the accumulation of sediment caused by the accumulation of rivers (Rong 2012).

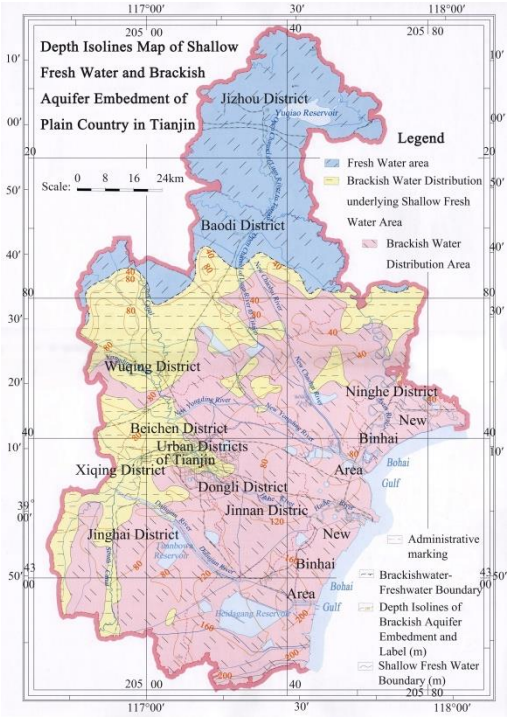

Figure 1. Depth Isolines Map of Shallow Aquifer Embedment of Plain Country in Tianjin, China

Tianjin is located in China's Bohai Rim plain, having abundant underground water and diverse hydrogeological structures. The whole Tianjin plain can be divided into the freshwater area, brackish water distribution underlying shallow freshwater area and brackish water area from north to south (Figure 1). In the structure of aquifer, the sandy layer transforms into medium coarse sand, medium sand, medium fine sand, fine sand and silty sand from north to south.

The distribution area of shallow underground brackish water in China's Binhai plain of Tianjin is 6,922 km^2, of which the brackish water area with a mineralization content of 2-3 g·L^{-1} and 3-10 g·L^{-1} are 3,753 km^2 and 3169 km^2 respectively, accounting for more than 2/3 of the city's total area (Zaiming 2012). Groundwater resources are rich in reserves and convenient for exploitation, but the hydraulic gradient and the natural seepage generally range from 1.3×10^{-2} m·a^{-1} to 12×10^{-1} m·a^{-1}. Therefore, CGSHP system is suitable in Tianjin plain.

2.2. Underground thermo-physical properties

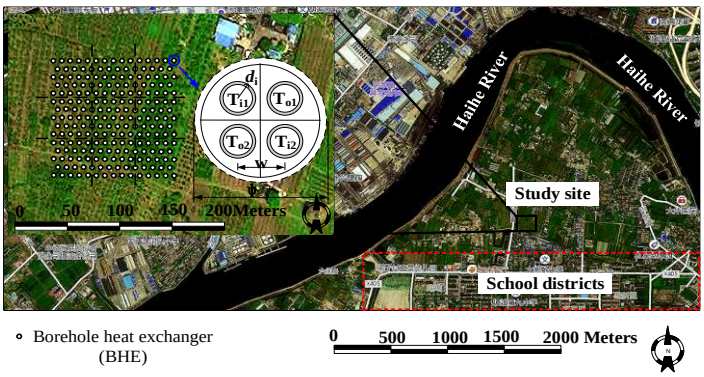

Figure 2. Location of study site in China, Tianjin, 2016 and plan view of BHEs

The GSHP system that installed in Tianjin Binhai New Area, China, 2016 is taken as the project prototype (Figure 2). The project has a research area of 150×120 m^2 and a vertical depth of -83m that it is divided into 5 geotechnical layers. Among whole study area, the fine sand layer has stronger permeability that is regarded as a well-developed confined aquifer, which

interacts with silty sand layer to form shallow-groundwater accumulation section. The geotechnical distribution and physical parameters are shown in Table 1.

Table 1. The physical parameters of the underground rock-soil layers

soil media	Depth of distribution σ (m)	horizontal permeability k_{XY} (m^2)	porosity ε_s	volumetric heat capacity of the soil $c_s\rho_s$ ($J\cdot m^{-3}\cdot K^{-1}$)	thermal conductivity λ_s ($W\cdot m^{-1}\cdot K^{-1}$)	longitudinal thermal dispersivity α_L (m)	transverse thermal dispersivity α_T (m)	Initial temperature of soil layer T_{S0}/℃
clay	0-9	$5.0\cdot10^{-14}$	0.45	$2.7\cdot10^{6}$	1.1	0.3	0.03	
silty clay	9-24	$5.0\cdot10^{-14}$	0.4	$3.2\cdot10^{6}$	1.2	0.3	0.03	
fine sand	24-44	$1.2\cdot10^{-12}$	0.35	$1.4\cdot10^{6}$	0.95	3.0	0.3	16
silty sand	44-80	$8\cdot10^{-13}$	0.38	$2.4\cdot10^{6}$	1.6	0.1	0.01	
silty clay	80-83	$5.0\cdot10^{-14}$	0.4	$3.2\cdot10^{6}$	1.2	0.3	0.03	

The project, which is mainly responsible for the energy supply of the adjacent school, contains 219 BHEs with a center-to-center spacing of 4-5 m. The vertical depth of the borehole is 83 m and the 2U-DN32-HDPE-BHEs with the length of 80 m is arranged in the well. The expansive soil with sand is selected as the grout materials. Water is selected as the circulating refrigerant in BHEs. The design parameters of BHEs are shown in Table 2.

Table 2. Design Parameters of 2U-Type BHE

Parameter/Symbol (Unit)	Value
BHE depth /H (m)	80
borehole diameter /ψ (m)	0.13
outer diameter of branch pipe-in(out)/$d_{i(o)}$ (m)	0.032
wall thickness of branch pipe-in(out)/$b_{i(o)}$ (m)	0.0029
adjacent branch pipe distance /w (m)	0.05
thermal conductivity of pipe-in(out) material/$\lambda_{pi(o)}$	0.6
thermal conductivity of refrigerant (water)/ λ_r	0.65
volumetric heat capacity of refrigerant (water) /$c_r\rho_r$	$4.18\cdot10^{6}$
volumetric heat capacity of grout/ $c_g\rho_g$ ($J\cdot(m^{-3}\cdot K^{-1})$)	$2.19\cdot10^{6}$
thermal conductivity of grout/ λ_g ($W\cdot m^{-1}\cdot K^{-1}$)	1.9

3. Heat-seepage coupling model

It is assumed that the seepage process of aquifer satisfies the following conditions: the physical parameters of aquifer and groundwater do not change with temperature; the seepage direction of groundwater is single and the vertical seepage process is ignored. According to the continuity equation of seepage flow and Darcy law (Nam and Ooka 2008), the continuity governing equation (1) and momentum governing equation (2) in the anisotropic and homogeneous aquifers are established:

$$[\varepsilon_s\gamma_f+(1-\varepsilon_s)\gamma_s]\frac{\partial h}{\partial t}+\nabla\cdot u_f=Q_\rho \tag{1}$$

$$u_f=-\frac{k\rho_f g}{\mu_f}\frac{\partial h}{\partial x} \tag{2}$$

In order to describe the change of heat transfer characteristics of BHEs in the aquifer under complex space-time conditions accurately on the basis of the convective-conduction equation (Antonio and Michele 2013), the control equation of three-dimensional unsteady convective - thermal dispersion is established by taking the thermal dispersion effect into account.

$$[\varepsilon_s\rho_f c_f+(1-\varepsilon_s)\rho_s c_s]\frac{\partial T}{\partial t}=-\rho_f c_f u_f\nabla\cdot T+\nabla\cdot[(\mathbf{\Lambda}^{\mathbf{cond}}+\mathbf{\Lambda}^{\mathbf{disp}})\nabla\cdot T]+Q_T \tag{3}$$

In which, the conductive part of thermodispersion tensor $\mathbf{\Lambda}^{\mathrm{cond}}$ and the dispersive part of thermodispersion tensor $\mathbf{\Lambda}^{\mathrm{disp}}$ are determined by equation (4) and (5) respectively.

$$\mathbf{\Lambda}^{\mathrm{cond}}=[\varepsilon_s\lambda_f+(1-\varepsilon_s)\lambda_s]\delta_{ij} \tag{4}$$

$$\mathbf{\Lambda}^{\mathrm{disp}}=\rho_f c_f\left(\alpha_T u_f\delta_{ij}+(\alpha_L-\alpha_T)\frac{u_{fi}u_{fj}}{u_f}\right) \tag{5}$$

The problem for determining solution of seepage flow is associated with the problem of heat transfer by the momentum equation (2), so the heat-seepage coupling model is constructed in the aquifer. The discharge (suction) heat process of the borehole can be considered as the source (sink) term in the aquifer thermal migration model. Because the diameter of the vertical borehole is much smaller than its depth, in order to consider effectively the influence of groundwater seepage on the heat transfer of BHE, the heat transfer process of BHE is simplified to the heat transfer process of the moving finite line heat source in the semi-infinite medium.

On the basis of considering the thermal dispersion effect and the spatial position of BHE, the moving finite line heat source model (MFLS) (Jin and Joachim 2013) is improved. Under the premise of constant heat flow rate per unit length of BHE, the optimized analytical model (Eq.6-7) is obtained by applying the method of images and the moving source theory. The optimized analytical model takes into account the heat convection, heat conduction and thermal dispersion effects in the process of groundwater seepage to determine the transient temperature in the aquifer caused by heat from the heat exchanger and is coupled with the internal heat transfer process of the borehole.

$$\Delta T(x,y,z,t)=\frac{q}{2\pi\sqrt{\lambda_x\lambda_y}}\exp\left[\frac{\rho_f c_f u_f(x-x')}{2\lambda_x}\right]\left[\int_0^H f(x,y,z,t)dz-\int_{-H}^0 f(x,y,z,t)dz\right] \tag{6}$$

$$f(x,y,z,t)=\frac{1}{4\sqrt{(x-x')^2+(y-y')^2+(z-z')^2}}\left[\exp\left(-\frac{\rho_f c_f u_f\sqrt{\frac{(x-x')^2}{\lambda_x\lambda_x}+\frac{(y-y')^2}{\lambda_x\lambda_y}+\frac{(z-z')^2}{\lambda_x\lambda_e}}}{2}\right)erfc\left(\frac{\sqrt{\frac{(x-x')^2}{\lambda_x\lambda_x}+\frac{(y-y')^2}{\lambda_x\lambda_y}+\frac{(z-z')^2}{\lambda_x\lambda_e}}\rho_e c_e-\frac{\rho_f c_f u_f t}{\lambda_x}}{2\sqrt{\frac{\rho_e c_e}{\lambda_e}t}}\right)\right.$$
$$\left.+\exp\left(\frac{\rho_f c_f u_f\sqrt{\frac{(x-x')^2}{\lambda_x\lambda_x}+\frac{(y-y')^2}{\lambda_x\lambda_y}+\frac{(z-z')^2}{\lambda_x\lambda_e}}}{2}\right)erfc\left(\frac{\sqrt{\frac{(x-x')^2}{\lambda_x\lambda_x}+\frac{(y-y')^2}{\lambda_x\lambda_y}+\frac{(z-z')^2}{\lambda_x\lambda_e}}\rho_e c_e+\frac{\rho_f c_f u_f t}{\lambda_x}}{2\sqrt{\frac{\rho_e c_e}{\lambda_e}t}}\right)\right] \tag{7}$$

In the analytic model, $\rho_e c_e$ is the volumetric heat capacity of the porous medium (Eq.8). When the thermal conductivity in the aquifers is the same in each direction, the thermal conductivity components of the $\mathbf{\Lambda}^{\mathrm{cond}}$ are determined by equation (9). λ_x and λ_y is the effective longitudinal and transverse thermal conductivity coefficient, respectively, which are determined by Eq.10 and Eq.11. r is the distance to the source located on the z-axis at the (x_0, y_0, z') coordinates (Eq.12).

$$\rho_e c_e=\varepsilon_s\rho_f c_f+(1-\varepsilon_s)\rho_s c_s \tag{8}$$

$$\lambda_x^{\mathrm{cond}}=\lambda_y^{\mathrm{cond}}=\lambda_z^{\mathrm{cond}}=\lambda_e=\varepsilon_s\lambda_f+(1-\varepsilon_s)\lambda_s \tag{9}$$

$$\lambda_x=\lambda_e+\alpha_L u_f\rho_f c_f \tag{10}$$

$$\lambda_y = \lambda_e + \alpha_T u_f \rho_f c_f \tag{11}$$

$$r = \sqrt{(x-x_0)^2 + (y-y_0)^2 + (z-z')^2} \tag{12}$$

When the thermal dispersion effect in the aquifer is ignored (λ_x=λ_y=λ_e), the excess temperature analysis model (Eq.6) and (Eq.7) can be simplified to Eq. 13 and Eq.14.

$$\Delta T(x,y,z,t) = \frac{q}{2\pi\lambda_e}\exp\left[\frac{\rho_f c_f u_f (x-x')}{2\lambda_e}\right]\left[\int_0^H f'(x,y,z,t)dz' - \int_{-H}^0 f'(x,y,z,t)dz'\right] \tag{13}$$

$$f'(x,y,z,t) = \exp\left(-\frac{\rho_f c_f u_f r}{2\lambda_e}\right) erfc\left(\frac{r\rho_e c_e - \rho_f c_f u_f t}{2\sqrt{\rho_e c_e \lambda_e t}}\right) + \exp\left(\frac{\rho_f c_f u_f r}{2\lambda_e}\right) erfc\left(\frac{r\rho_e c_e + \rho_f c_f u_f t}{2\sqrt{\rho_e c_e \lambda_e t}}\right) \tag{14}$$

4. Experimental System

In order to ensure the reasonable use of the limited laboratory indoor space, the fine sand layer, which was a typical hydrogeological medium in shallow the aquifer, with the area of 20×16m² and the buried depth of 24~44m in Figure 2 were selected as the engineering prototype for designing and building a complete laboratory experimental system. The engineering prototype contained 6 ordinals arranged BHEs with the tube pitch of 4m.

4.1. Design and Construction of Experimental system

The experimental system consists of a sandbox, a heating apparatus, a flow conditioning apparatus and a data-acquisition apparatus (Figure 3). Since the seepage and heat transfer processes in the seepage sandbox and the engineering prototype followed the same form of governing equations (Eq.1-3), the similitude relation ratio of basic design parameters was determined by equation analysis method according to the principle of similarity criteria (Min and Alvin 2015; Mao and Prommer 2006).

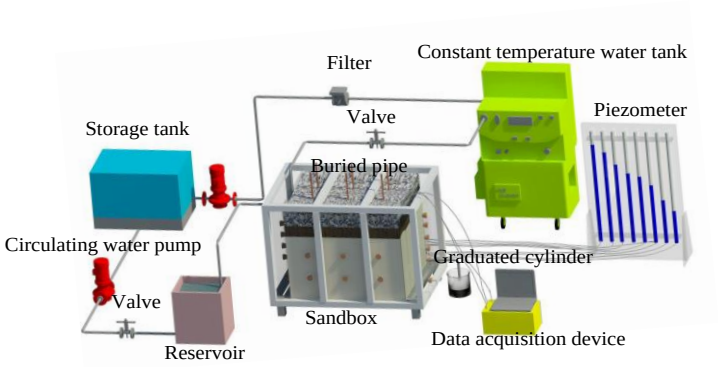

Figure 3. Schematic diagram of the experimental system

The proportional relationship between hydrogeology and thermophysical parameters of aquifers was 1:1 due to the use of equal volumetric weight filling of raw sand and seepage of raw water. In order to shorten the experimental period, the proportional relationship between the heat intensity of BHEs and the difference of water head was set as 1:1. The geometric size proportional relationship between the actual and experimental was determined as 20:1. The *Pr* (Eq.15), *Fo* (Eq.16) and *Pe* (Eq.17) in the engineering prototype and the sandbox were required to be equal in order to ensure that the experimental system can reproduce effectively the heat-seepage migration process of the aquifer. Thus, the operation time proportional relationship between the actual and the experimental was determined to be 400:1 and the seepage velocity proportional relationship between the actual and the experimental was determined to be 1:20, so as to determine other design parameters, as shown in Table 3.

$$Pr = \frac{\rho_f \rho_e c_e}{\mu_f \lambda_e} = \frac{\rho_{fm} \rho_{em} c_{em}}{\mu_{fm} \lambda_{em}} = Pr_m \tag{15}$$

$$Fo = \frac{\lambda_e t}{\rho_e c_e l^2} = \frac{\lambda_{em} t_m}{\rho_{em} c_{em} l_m^2} = Fo_m \quad (16)$$

$$Pe = \frac{\rho_f c_f u l}{\lambda_e} = \frac{\rho_{fm} c_{fm} u_m l_m}{\lambda_{em}} = Pe_m \quad (17)$$

Table 3. Engineering prototype and experimental system design parameters

classify	volume $x \cdot y \cdot z$ (m^3)	pressure diaphragm thickness σ_1 (m)	confined aquifer (fine sand layer) thickness σ_2 (m)	tube pitch l(m)	heat transfer rates per unit borehole depth q ($W \cdot m^{-1}$)	Darcy velocity u_f ($m \cdot s^{-1}$)	operation time t
prototype	20×16×20	4	12	4	50	1.2×10^{-7}	90d
test-bed	1.0×0.8×1	0.2	0.6	0.2	50	2.4×10^{-6}	5.4h

According to the geometric similarity ratio, the sandbox was set to 1.2×0.8×1.2 m^3 while the seepage region was 1×0.8×1 m^3 and the confined aquifuge region was 1×0.8×0.2 m^3. The liquid supply/discharge region was 0.1 ×0.8 ×1.2 m^3, which was symmetrically set at both ends. Then five overflow holes (Φ20 mm) with spacing of 0.2m were drilled in the centerline of plexiglas's plate on the outsides of the liquid supply/discharge region. During the experiment, rubber plugs of overflow holes at different heights were opened to control the hydraulic difference between the liquid supply/drainage region, so as to change the seepage velocity in the seepage region. Plexiglas's plate with the equally distributed holes (Φ5 mm) was installed between liquid supply/discharge region and the seepage area to ensure that the seepage solution flows horizontally and evenly in the aquifer.

The K-type (±0.1℃) thermocouple treated with waterproof and anti-corrosion package was selected to measure aquifer temperature. Nine K-type thermocouples were embedded 0.5m away from the bottom of the sandbox. The data acquisition apparatus was used to record temperatures of the aquifer. Then, six PPR pipes with 1.5m-long, which fixed on the bottom plate of the sandbox, were wound evenly with electric heating wire (50W/m) to simulate the BHEs as the heat source device of the sandbox. The plane layout of BHEs and temperature observation points was shown as Figure 4.

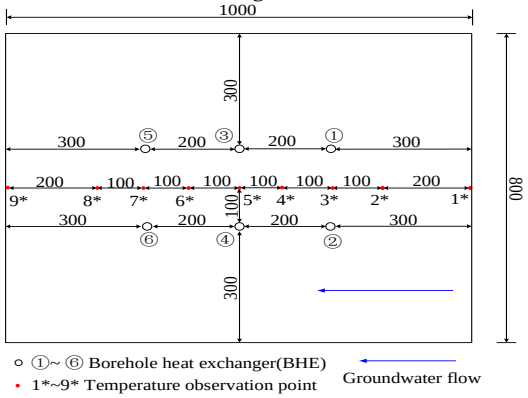

Figure 4. Layout of BHEs and temperature observation points (unit: mm)

The precision bath circulator THD-3015 was selected as the cold/heat source equipment in order to ensure that the temperature of the circulating groundwater meets the requirements of the test. Furthermore, the thermal insulation materials with the thickness of 0.15 m were attached to the outside of the sandbox device, connecting pipes, storage tank and reservoir. After pasting thermal insulation materials, six K-type thermocouples were fixed respectively on all six sides of the sandbox to measure the heat loss of the experimental system.

4.2. Experimental scheme

The sand sample and the groundwater were collected in the aquifer at the underground depth of 24~44m in the relevant project. The sandbox was filled with equal volumetric weight by layered wet filling method. Each raw sand layer with a thickness of 50mm was filled while the raw underground water was sprayed evenly and the sand layer was compacted to ensure that the porous medium in the sandbox has unit weight of 1.68±0.1 kg·L^{-1}, which was similar to that of the underground aquifer. The filling height of raw sand was 1m, and then the upper part of the sandbox was laid with a 0.2m clay-gravel layer as the confined aquifuge to isolate the aquifer from the external environment. The photograph of the sandbox without the thermal insulation material was shown as Figure 5.

Figure 5. Photograph of the infiltration sandbox

After the establishment of the experimental system, the room temperature was first maintained at 18℃ by central air conditioning, and then the 16℃ underground raw water was filled into the sandbox for the exhaust gas process of porous media. When all temperature observation points in the sandbox were maintained at 16±0.1℃, and the water level in the piezometer was stable and no bubbles appeared, the porous medium of the sandbox could be considered as saturated aquifer.

Before the experiment, it was proved that Darcy velocity was 2.4±0.02×10^{-6} (Pe≈2.5) when the hydraulic difference was 0.2m, which satisfied the proportional relationship between actual and experimental seepage velocity 1:20. During the experiment, the 16℃ underground raw water with 0.2 m hydraulic difference was filled continuously into the sandbox to ensure a stable Darcy velocity, simultaneously, BHEs ①~④ were opened in the test. The experimental run time was set at 5.4 h and the temperature of each observation point was recorded per 1 min. Through the experiment, it was found that the temperature measurement range of the six thermocouples outside the thermal insulation sandbox was 18±0.5℃, so the heat loss from the sandbox was in negligible level.

5. Numerical Simulation Verification

5.1. Compared with analytical and experimental data

According to the engineering prototype, FEFLOW 7.1 is used to establish the geometric model, mesh division (triangular element non-equidistant) and set the parameters, and then perform numerical simulation calculations. Meanwhile, MATLAB 2012 is used to calculate the transient temperature response caused by the running BHE in engineering prototype, according to the unsteady analytical model of the excess temperature in the aquifer (Eq.6-7). Then, the experimental result and the analytical solution of the engineering prototype are compared with the numerical solution of the engineering prototype.

In the numerical simulation, the clay layer is defined as a confined aquifuge while the fine sand layer with a thickness of 20m exists as a confined aquifer. The clay layer in the

upper part of the study area is defined as the impervious and adiabatic boundary while the external environmental impact is ignored. Moreover, the four flanks of the 20×16×83 m^3 model are defined as the fixed hydraulic head and constant temperature boundary. Then, the parameters of the six ordinals arranged BHEs in this area are set according to Table 2. In addition, the triangular element non-equidistant mesh generation is adopted in the entire geotechnical layer. The physical model has a total number of nodes of 51740 and a grid number of 93156. The fixed-time step method is used in the solution process. The total number of time steps is 324 when the time-step length is set to 1 min and the maximum iteration is 2500 times per step.

For facilitating the comparison, the time t, the excess temperature ΔT and the coordinate displacement x are all in a dimensionless form. Due to the different proportional relationship between the engineering prototype and the experimental system in operation time and geometric size, Fo is taken as dimensionless time (Eq.16), θ is taken as dimensionless excess temperature (Eq.18) and L is taken as dimensionless coordinate displacement (Eq.19). Meanwhile, the root mean square error (RMSE) of dimensionless excess temperature θ (Eq.20) is selected as the similarity index between experimental results, analytical solutions and numerical solutions.

$$\theta = \frac{4\pi\lambda_e \Delta T}{q} \tag{18}$$

$$L = \frac{x}{l} \tag{19}$$

$$\mathrm{RMSE} = \sqrt{\frac{\sum_{i=1}^{n}(\theta_{N(i)/A(i)} - \theta_{E(i)})^2}{n}} \tag{20}$$

in which $\theta_{N(i)/A(i)}$ corresponds to the numerical solutions and analytical solutions respectively, and $\theta_{E(i)}$ corresponds to the experimental result.

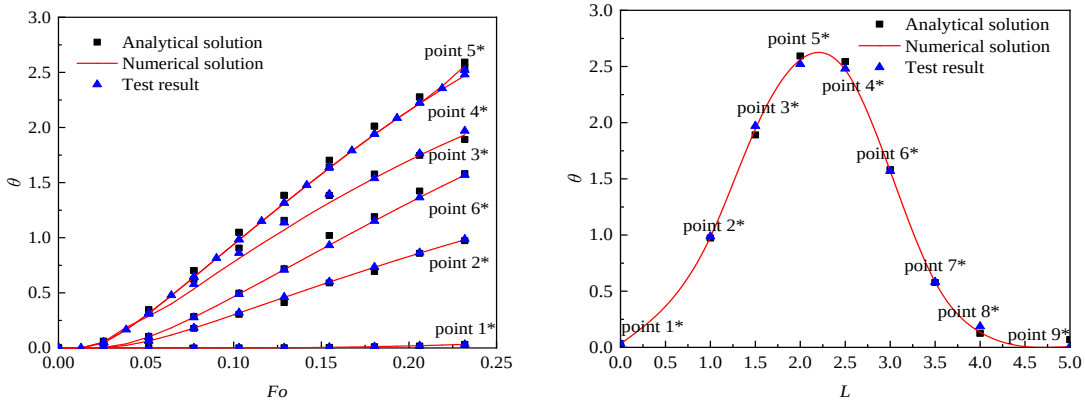

Figure 6. Comparison of multi-tube (Four-tube) analytical solution and numerical solution with experimental result (y=0m,z=0.5m) :(a) temperature response θ over Fo (the observation points 1*~6*); (b) temperature response θ over dimensionless distance L (Fo=0.232)

The RMSE between the analytical solutions and the experimental results in Figure 6(a) does not exceed 5% while the RMSE between the numerical solution and the experimental result does not exceed 1%. Besides, the RMSE between the analytical solution and the experimental result is 3.8% and the RMSE of the numerical solutions and experimental results is 0.5% in Figure 6(b). The results show that the analytical solution and experimental results are consistent with the numerical solution, so FEFLOE 7.1 can simulate effectively and accurately the heat transfer process of BHEs in the aquifer.

5.2. Compared with existing studied data

The numerical solutions regarding the mean temperature change of the aquifer are then compared to available data derived from [11]. Since the studies in literature refer to different ground properties and groundwater velocities, as well as to different dimensions, the comparison is performed by calculating for each condition in the papers the *Pe*, *Fo*, $\bar{\theta}$.

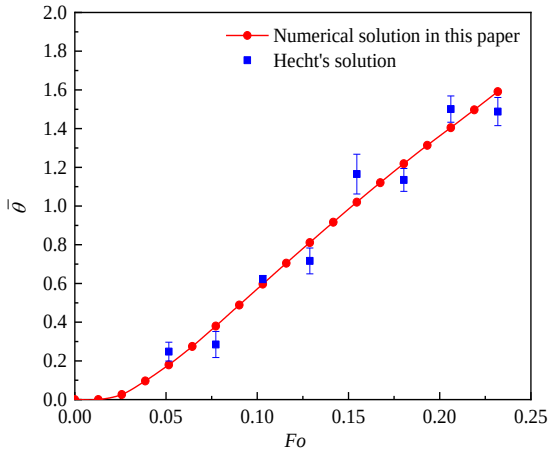

Figure 7. Comparison of multi-tube (Four-tube) numerical solution with Hecht's solution [11]: dimensionless mean temperature ($\bar{\theta}=4\pi\lambda_e\Delta\bar{T}/q$) change over *Fo*

Table 4. Comparison between the numerical solutions and the Hecht's solution in: $\bar{\theta}$ and relative error for *Fo*

Fo	$\bar{\theta}$	Fit standard mean deviation	$\bar{\theta}$ relative error (%)
0.05153	0.17937	0.248	4.9%
0.07729	0.37967	0.2846	-6.7%
0.10306	0.59666	0.62288	1.9%
0.12882	0.81075	0.7164	-6.7%
0.15459	1.01956	1.165	10.3%
0.18035	1.21858	1.1348	-5.9%
0.20612	1.40478	1.5009	6.8%
0.23188	1.59073	1.48792	-7.3%

After comparing *Pe*, it is found that the "scenario 12" in Hecht's research [11] are close to the working conditions in this paper (Figure 7). The results show that the maximum error is 10.3% and the other errors are less than 10%. Therefore, using FEFLOW7.1 to simulate the heat transfer process of the BHEs under forced seepage is effective and correct.

6. Analysis of examples

This section explores the influence of the pumping-injection flow rate of CGSHP system compared with the established traditional GSHP system (Figure 2) on enhancing the heat transfer effect.

6.1. Generalized model and Operation scheme

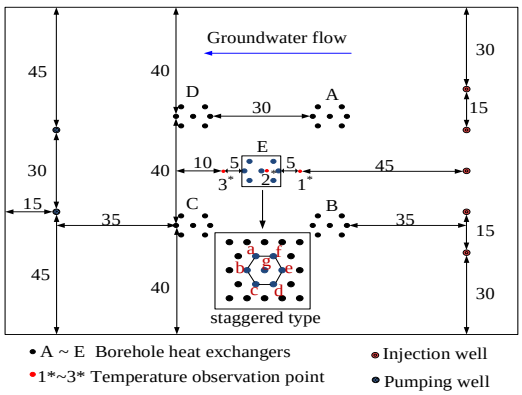

Figure 8. Geometric arrangement of BHEs and pumping - injection wells (unit: m)

Because of the complex and diverse layout of the on-site well group and a large number of boreholes, the BHEs (Figure 2) are generalized into five groups of BHEs in Figure 8. For

each group, there are seven boreholes arranged according to a staggered layout while the space between each borehole is 4~5 m. To ensure the groundwater synchronous recharge, two pumping wells and five injection wells are set up. Moreover, the design parameters of BHE are shown in Table 2. The seven working wells are all incomplete diving wells with a depth of 60 m and a diameter of 0.4 m. Meanwhile, the filter is placed at a depth of 40~50 m.

On the grounds of the layout of the well group, the horizontal calculation area is 150×120 m^2 and the vertical calculation range is 0~-83 m. From the top to the bottom, the rock-soil layer with a thickness of 83 m is separated into five types of horizontal fault. The spatial distribution and physical properties of that layer are shown in Table 1.

In the numerical calculation, the silty clay layer in the upper and lower part of the study area is defined as the impervious and adiabatic boundary as the effects of atmospheric rainfall and evaporation are ignored. The four flanks of the physical model are defined as the fixed hydraulic head and constant temperature boundary. In addition, the pumping-injection wells are defined as the constant flow boundary. The triangular element non-equidistant mesh division is adopted for each rock-soil layer. Local refinement of the mesh is set in the location of BHEs and the pumping-injection wells.

The number of total nodes and grid in the physical model is 248,752 and 413,295. The fixed-time step method is used in the solution process. The time step, the total time step and the maximum iteration are set to 1d, 3650 and 2500(times per step) respectively. Based on the established model, the simulation calculations are carried out for eight kinds of operation modes respectively (Table 5).

Table 5. Operation scenarios of the coupling pumping-injection wells and BHEs

Scenario	Total flow rate of refrigerant per borehole ($m^3 \cdot d^{-1}$)	Pumping quantity of single well ($m^3 \cdot d^{-1}$)	Rated power of the submersible pump kW	Recharge quantity of single well ($m^3 \cdot d^{-1}$)	Rated power of the pressure pump kW
1	30	0	0	0	0
2	30	100	1.5	40	0.75
3	30	200	2.2	80	1.1
4	30	300	4	120	2.2
5	30	400	5.5	160	2.2
6	30	500	5.5	200	3
7	30	600	7.5	240	3
8	30	700	7.5	280	3

To divide one operation cycle (1 year) into four stages that are followed by summer cooling stage (4 months), autumn intermittent stage 1 (2 months), winter heating stage (4 months) and spring intermittent stage 2 (2 months). The system runs five operation cycles and BHEs operate continuously for 10 hours per day in both the cooling and heating stage. The inlet water temperature of BHEs during cooling/heating stage is constant at 31℃ /6℃ is respectively.

6.2. Analysis and discussion

The Darcy velocity and the hydrodynamic distribution have a significant difference in the same aquifer since the total pumping-injection flow rate (∑G) is different (Figure 9). Darcy

velocity, which increases approximately 10 time, increases from 2.4 ~ 3.2×10^{-7} m·s^{-1} to 2.0~3.0×10^{-6} m·s^{-1} When the total pumping-injection flow rate increases from 200 m^3·d^{-1}to 1200 m^3·d^{-1}.

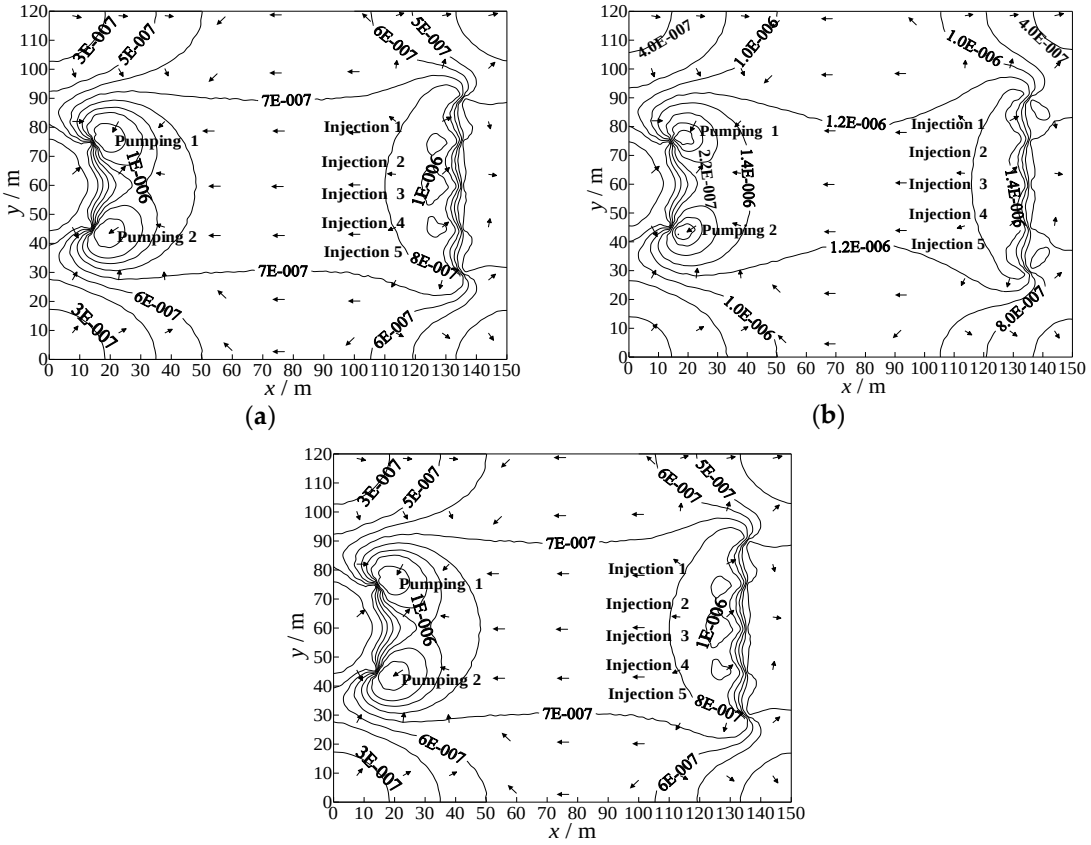

Figure 9. Spatial hydrodynamic distribution in the fine sand layer on the 120d under the different total pumping-injection flow rate ∑G: (a) ∑G=200 m^3·d^{-1}; (b) ∑G=600 m^3·d^{-1}; (c) ∑G=1200 m^3·d^{-1}

Due to the difference of pumping-injection flow rate, profile temperature fields have a significant difference in the same aquifer (Figure 10). Taking BHEs' well group E as the research object, the injection well and the pumping well with a spacing of 120 m are defined as the upstream and downstream boundaries, respectively.

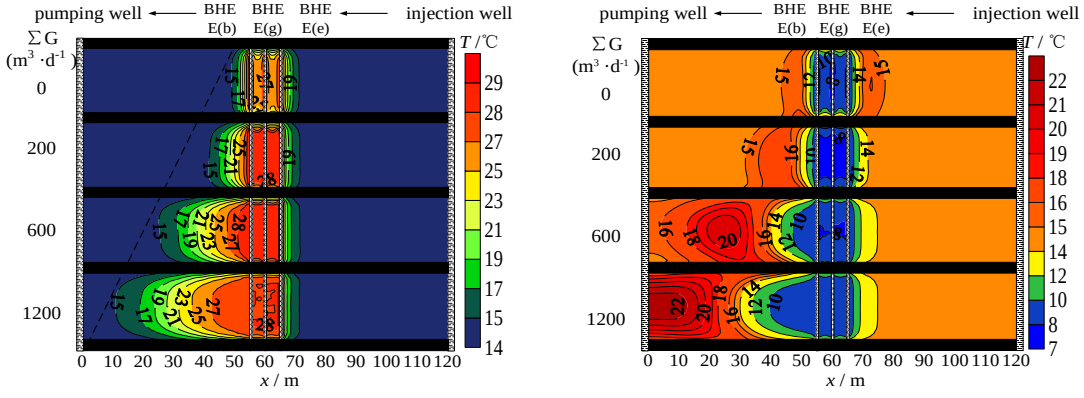

Figure 10. Profile temperature field in the fine sand aquifer under the different total pumping-injection flow rate: (a) the end of the cooling stage (120 d); (b) the end of the heating stage (300 d)

To describe accurately the evolution process of the aquifer's temperature field under different operation modes, the calculation area with a temperature change of ±0.5 ℃ is defined as the thermal diffusion range of the BHEs. Besides, the heat-influencing radius is defined as the coordinate distance between E (g) and the farthest acting position.

When the pumping-injection flow rate is 0 $m^3 \cdot d^{-1}$, there is only the heat conduction between BHEs and the aquifer as well as between the aqueous medium units. The heat transfer process is slow and the heat influence range is diffused symmetrically around BHEs. By the end of the cooling stage (120d), the thermal radius of BHEs in both upstream and downstream areas is 11 m.

The range of thermal diffusion in the downstream area of BHEs significantly expands with the pumping-injection flow rate increases from 200 $m^3 \cdot d^{-1}$to 1200 $m^3 \cdot d^{-1}$. At the 120 d, the thermal radius along the direction of pumping reaches 19 m, 35 m and 49 m, so the thermal radius of 1200 $m^3 \cdot d^{-1}$ is 2.6 times of that of 200 $m^3 \cdot d^{-1}$. With the increase of the flow rate, the migration speed of the temperature fronts accelerates and the thermal radius enlarges continuously, moreover, the thermal radius in the upstream zone is smaller than 11m.

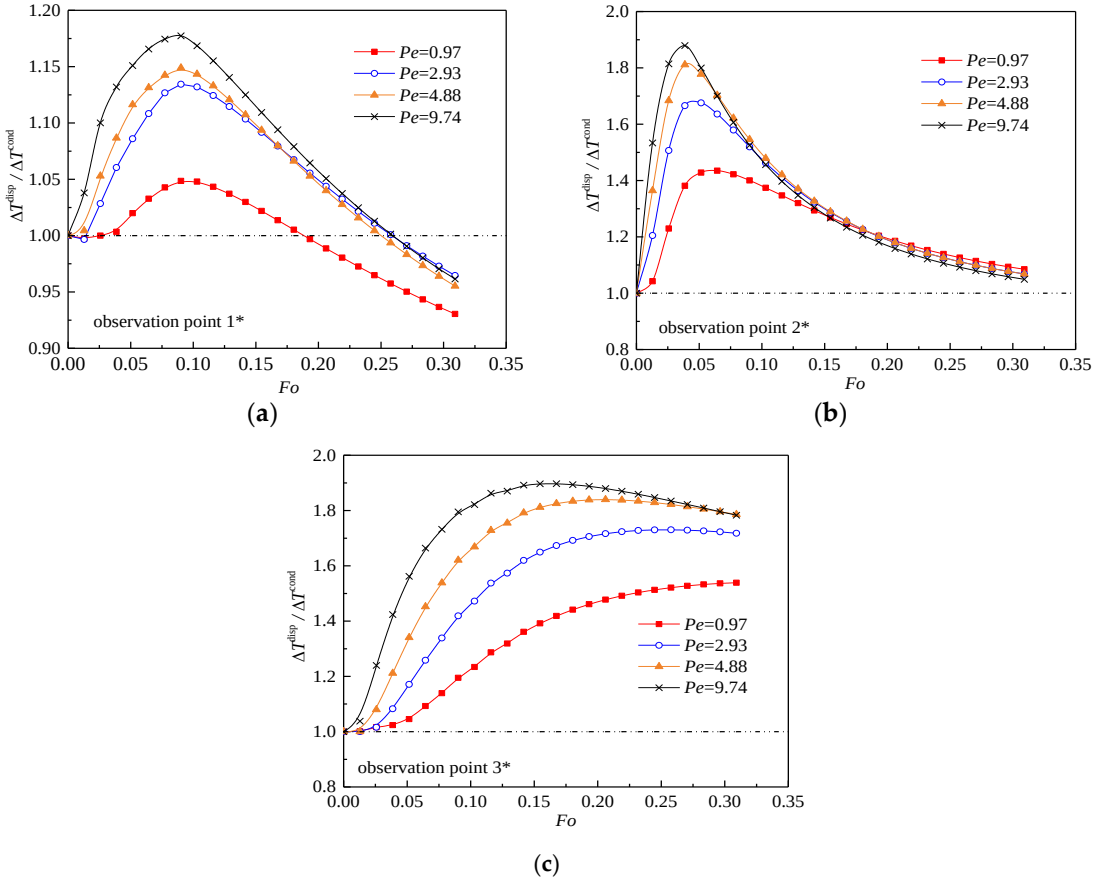

Figure 11. Temperature response dynamic curve in the fine sand aquifer at the first cooling stage: (a) the upstream area of BHEs (the observation point 1*); (b) the inside area of BHEs (the observation point 2*); (c) the downstream area of BHEs (the observation point 3*)

According to the theory of heat and mass transfer, it is precisely because of the increase of Darcy velocity that the convective heat transfer intensity and thermomechanical dispersion effect are improved correspondingly, thereby expanding the range of thermal diffusion in the downstream region and alleviating the thermal accumulation phenomenon of BHE. So, in order to obtain the difference between the temperature response ΔT^{disp} with forced

groundwater seepage and the temperature response ΔT^{cond} without groundwater seepage at different temperature observation points, the dynamic variation of $\Delta T^{disp}/\Delta T^{cond}$ with time is calculated (Figure 11).

As shown in Figure 11 (a), the mutative extent of temperature decreases gradually with the running time. When the running time exceeds 50% of the whole period ($Fo \geq 0.2$), $\Delta T^{disp}/\Delta T^{cond} < 1$. As shown in Figure 11 (b), $\Delta T^{disp}/\Delta T^{cond}$ tends to be stable gradually with time. At the end of the cooling stage(120d), $\Delta T^{disp}/\Delta T^{cond} > 1$. The change of Darcy velocity has no obvious influence on the change rate and amplitude of excess temperature because the thermal convection and thermal dispersion enhances thermal interference between BHEs. As shown in Figure 11 (c), with the passage of time, the excess temperature tends to be stable and the curve of $\Delta T^{disp}/\Delta T^{cond}$ tends to be smooth. The mutative degree of excess temperature enhances with the increase of Darcy velocity but the difference between ΔT^{cond} and ΔT^{disp} tends to decrease when Darcy velocity increases to a certain extent.

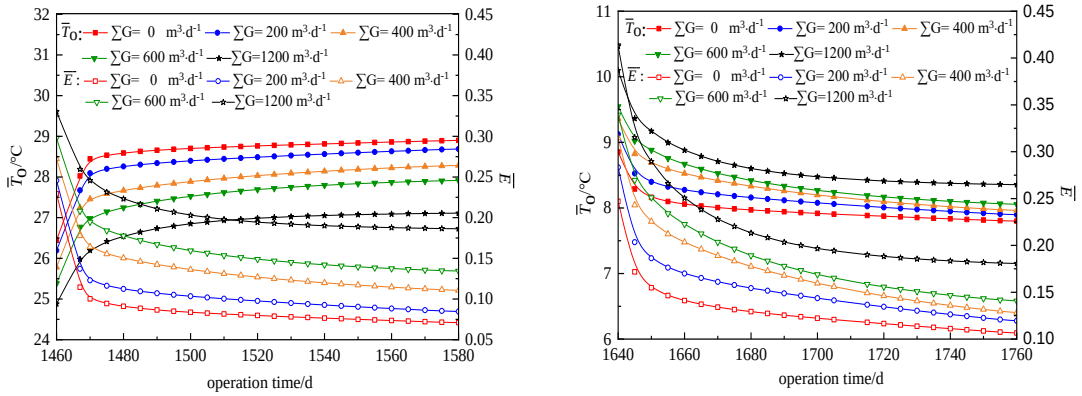

Figure 12. Dynamic changes of the average outlet water temperature ($\bar{T}_O$) and the average heat transfer efficiency ($\bar{E}= \bar{Q}/\bar{Q}'=|\bar{T}_i-\bar{T}_o|/|\bar{T}_i-\bar{T}_{s0}|$) of BHEs in the fifth operation cycle: (a) the cooling stage; (b) the heating stage

At the early stage of various operation modes, due to the large temperature difference in heat transfer between the boreholes and the rock-soil layer, the temperature difference between the inlet with outlet water of BHEs is higher and the corresponding energy efficiency coefficient also rise, (Figure 12). The heat exchange rate reduces because of the decreasing temperature difference between the boreholes and the surrounding medium. As a result, the temperature difference of the inlet and outlet water of BHEs decreases rapidly. At the end of the fifth operation cycle, the average heat transfer efficiency of the five types of operation modes in the cooling stage is 7.1%, 8.5%, 11.1%, 13.4% and 18.6% while the average heat transfer efficiency in the heating stage is 10.6%, 11.9%, 12.8%, 14.6% and 18.1% respectively.

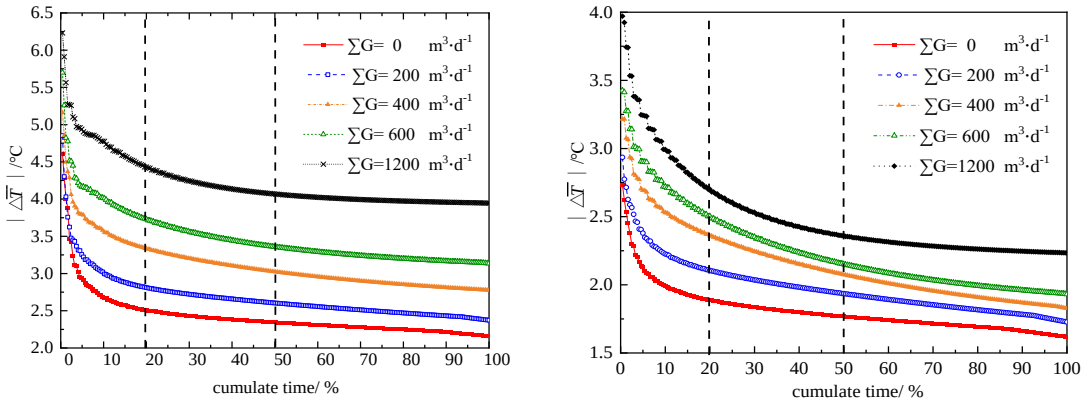

Figure 13. Cumulative distributions of the temperature difference of the inlet and outlet water of BHEs: (a) the cooling stage; (b) the heating stage

The cumulative distribution curve can be used as another evaluation index to describe the duration of a certain heat exchange efficiency of BHEs (Figure 13). The absolute values of the inlet and outlet temperature difference of BHEs is arranged in descending order, and the cumulative average temperature difference distribution in the cooling stages and heating stages over the whole simulation stages (5 years) is calculated. When the cumulate time exceeds 20% of the total operation stage, the temperature difference tends to be moderate, when the cumulate time reaches 50% and the temperature difference reaches a steady state.

The inlet and outlet temperature difference of BHEs corresponding to the median time is used as another evaluation index to compare the heat transfer performance of BHEs under different modes. In cooling stage, the median of temperature difference is 2.34℃ when the pumping-injection flow rate is 0 $m^3 \cdot d^{-1}$. With the pumping-injection flow rate rises from 200 $m^3 \cdot d^{-1}$ to 1200 $m^3 \cdot d^{-1}$, the growth rate of the median temperature difference varies from 11.5% to 73.9%. In heating stage, the median temperature difference is 1.76℃ when BHEs run individually.With the pumping-injection flow rate increases from 200 $m^3 \cdot d^{-1}$ to 1200 $m^3 \cdot d^{-1}$, the growth rate of the median temperature difference increases from 10.2% to 34.1%. As the pumping-injection flow rate, Darcy velocity and the heat exchange intensity of BHEs all increase, thereby the decline rate of the temperature difference slows down while the time required reaching a steady state increase.

The heat transfer rates per unit borehole depth of BHEs ($\bar{q}$) rise gradually when pumping and injection flow rate increases (Figure 14). Taking the fifth year as an example, the $\bar{q}$ in cooling and heating stages with the increase of the pumping-injection flow rate from 0 $m^3 \cdot d^{-1}$ to 1200 $m^3 \cdot d^{-1}$ varies from 30.3 $W \cdot m^{-1}$ and 25.4 $W \cdot m^{-1}$ to 82.2 $W \cdot m^{-1}$ and 39.6 $W \cdot m^{-1}$ respectively.

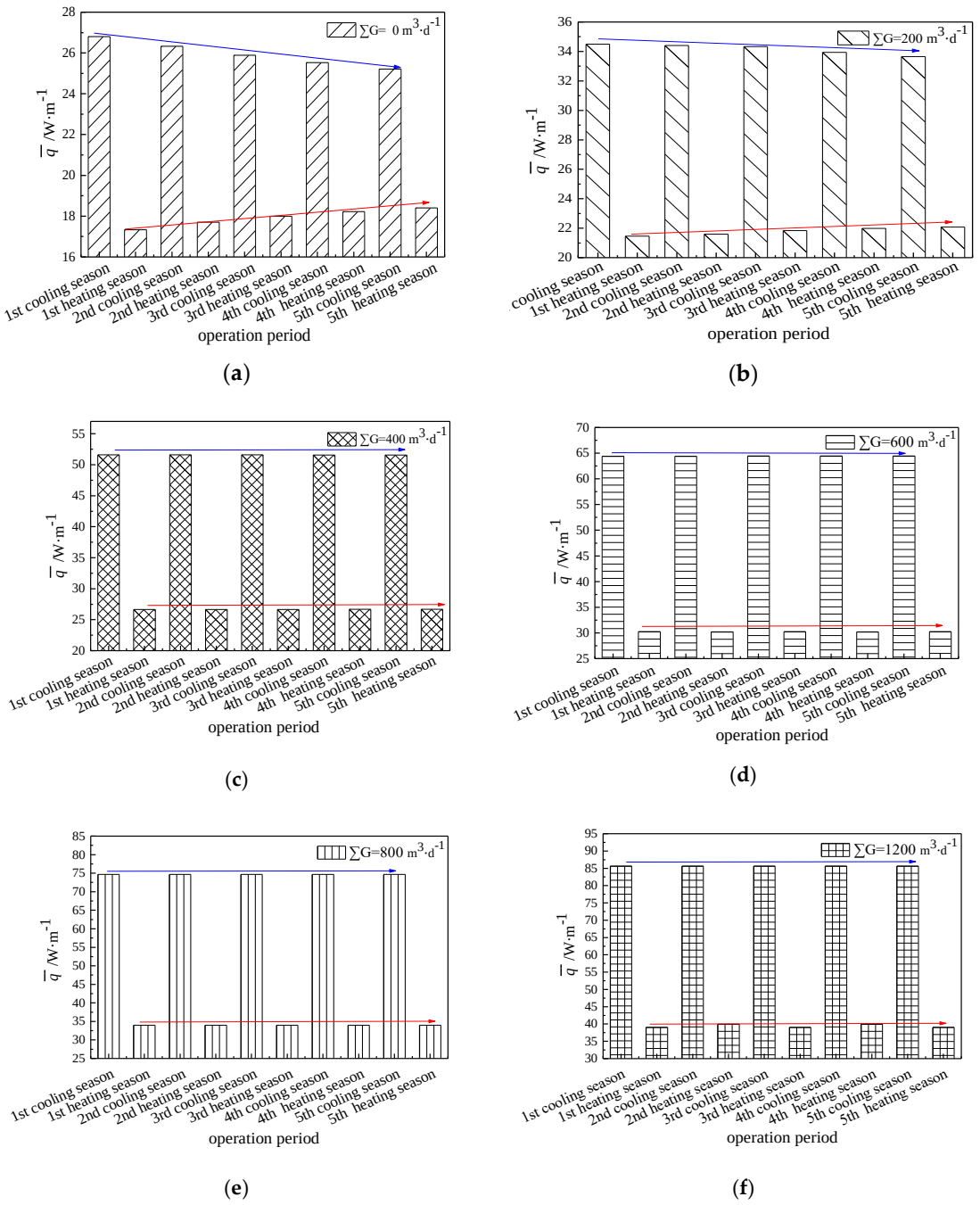

Figure 14. Average heat transfer rates per unit borehole depth of BHEs ($\bar{q}=(\rho_r c_r M\Delta\ \bar{T})/H$) in the fine sand layer over the whole operation period under different pumping-injection flow rate ∑G: (a) ∑G=0 $m^3 \cdot d^{-1}$; (b) ∑G=200 $m^3 \cdot d^{-1}$; (c) ∑G=400 $m^3 \cdot d^{-1}$; (d) ∑G=600 $m^3 \cdot d^{-1}$; (e) ∑G=800 $m^3 \cdot d^{-1}$; (f) ∑G=1200 $m^3 \cdot d^{-1}$

Thermal accumulation becomes serious with the continuous operation of the system, then the average heat transfer efficiency gets lower on the condition that the pumping and injection well ceases to work or the pumping-injection flow rate come to be smaller (200 $m^3 \cdot d^{-1}$). As a result, cooling and heating quantity is declining every year. However, the rock-soil layer is not a single cold or heat source while an energy storage body has certain thermal storage and rejection. Therefore, thermal accumulation in the wells group's area enhances the heat storage capacity of the rock-soil layer across the season in the summer. During the heating stage, the temperature of the rock-soil layer is higher than the initial stage.

The temperature difference between the soil and the circulating solution increases so that the heat exchange quantity of the BHEs is improved at this stage.

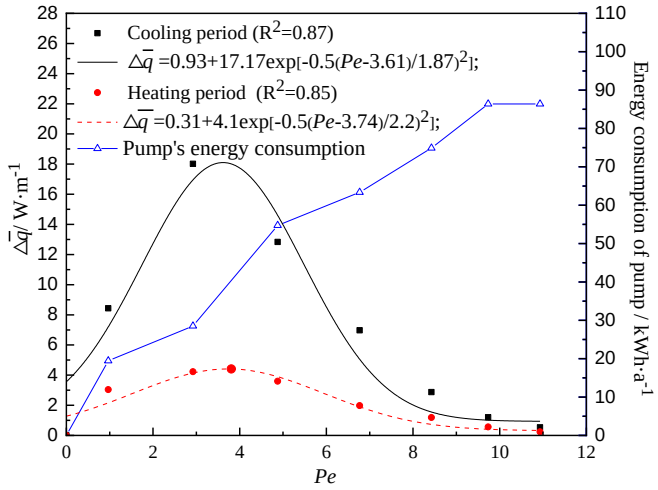

Figure 15. The total energy consumption of pumps and the increment of heat transfer rate per unit depth of BHEs ($\Delta\ \bar{q}$= $\bar{q}_{t+1}$- $\bar{q}_t$) change over *Pe*

Under the cooling and heating stages, the relation between $\Delta\ \bar{q}$（known as the increment of average heat transfer rate per unit depth of BHEs）and *Pe* is determined by fitting which shows that $\Delta\ \bar{q}$ is distributed as a Gaussian function with the uptrend of *Pe* (Figure 15). Although the effect of convective heat transfer and thermal dispersion between BHEs and the rock-soil layer can be enhanced effectively by strengthening the velocity of groundwater seepage, the average heat transfer rates per unit borehole depth of BHEs $\bar{q}$ does not raise linearly with the increase of the pumping-injection flow rate.

The research shows that Darcy velocity is only 0.6×10^{-6}~1.4×10^{-6} m·s^{-1} when the pumping and injection flow rate is 400~600m^3·d^{-1}, but the $\Delta\ \bar{q}$ respectively reaches 12.8~17.9W·m^{-1} and 3.6~4.2 W·m^{-1} during the cooling stage and heating stage which are located on both sides of the extremum point of the distribution curve. As the designed Pumping-injection flow rate further increases, not only the $\Delta\ \bar{q}$ decreases gradually, but also the energy consumption of pumping and injection pumps increase that leads to the increase of operation cost of the system. Furthermore, the change of aquifer spatial structure will be irreversible if the forced seepage velocity is too high. Therefore, in order to obtain the best heat transfer enhancement effect, system environment and economic benefits, the pumping-injection flow rate when Darcy velocity reaches 0.6×10^{-6}~1.4×10^{-6} m·s^{-1} is taken as the best reference range for CGSHP system, so the best flow rate range of pumping-injection wells is 400~600 m^3·d^{-1} in this paper.

7. Conclusion

In this paper, CGSHP system is proposed as the same as the effect of the flow rate of pumping and injection wells on heat transfer characteristic of BHEs is studied for this system. The main conclusions of this study can be summarized as follows:

(a) For CGSHP system, an indoor sandbox is built by equation analysis method according to the principle of similarity criteria. At the same time, the equal volumetric weight by layered wet filling method is adopted to ensure that the porous medium in the sandbox is similar to that of the underground aquifer. So, the sandbox experiment could effectively reproduce the process of forced seepage and convection heat transfer in the aquifer. The

sandbox experiment and analytical model are used to verify the numerical simulation of FEFLOW7.1. The results show that the numerical simulation software FEFLOW7.1 can simulate effectively and correctly the evolution process of the aquifer temperature field during the taking heat of BHEs.

(b) When the pumping-injection flow rate from 200 $m^3 \cdot d^{-1}$ to 1200 $m^3 \cdot d^{-1}$, Darcy velocity in the fine sand layer increases approximately 10 times and the effect of convective heat transfer and thermal dispersion is enhanced. In the downstream region of BHEs, the thermal action radius is 2.6 times of the original radius. Hence, the cold and heat accumulation of CGSHP system can be alleviated effectively in the aquifer.

(c) For long-term running BHEs, the cumulative distribution curve of the inlet and outlet water average temperature difference is introduced to describe the duration of a certain heat exchange efficiency of BHEs. The average temperature difference corresponding to the median time is used as a new parameter for evaluating the heat transfer performance of BHEs. When the flow rate of pumping-injection wells increases, the average temperature difference and the average energy efficiency coefficient of BHEs as well as the heat exchange quantity of BHEs are improved substantially.

(d) In cooling and heating stages, the relation curve between the $\Delta \bar{q}$ and Pe has a Gaussian function distribution. Therefore, the heat exchange quantity of BHEs cannot be increased continuously by increasing the pumping-injection flow rate infinitely. The pumping-injection flow rate that can make Darcy velocity reaches 0.6×10^{-6}~1.4×10^{-6} $m \cdot s^{-1}$ is the best reference range of CGSHP system，so the best pumping-injection flow rate is 400~600 $m^3 \cdot d^{-1}$ in this paper.

(e) CGSHP system is proposed for the areas where the shallow-groundwater reserves are abundant but the seepage velocity is weak, such as the Bohai Plain in Tianjin, China. The results show that the system can control the seepage velocity of groundwater by changing the pumping-injection flow rate to enhance heat transfer, so CGSHP system has good controllability and predictability. In addition, CGSHP system should also be applicable to other countries with the same hydrogeological conditions as the region in this paper. The system has certain universality.

8. Declarations

Author contributions: JM and QJ performed conceptualization; JM and QJ performed data curation; JM and QJ performed formal analysis; JM and QJ provided methodology; QZ provided resources; YX and YW provided software simulation; FY validated data; QJ writed the original draft; JM and QJ improved and revised the manuscript. All authors read and approved the final manuscript.

Funding: This research was funded by National Natural Science Foundation of China of Funder, grant number 41402228; This research was funded by Enterprise science and technology commissioner project of Tianjin of Funder, grant number 19JCTPJC48100.

Availability of data and materials: The datasets generated and analyzed during the current study are available from the corresponding author on reason-able request.

Acknowledgments: Thanks to the Tianjin Institute of Geotechnical Investigation Surveying for the hydrogeological parameters and relevant data provided.

Conflicts of Interest: The authors declare that they have no competing interests.

Author details: [1] School of Energy Safety Engineering, Tianjin Chengjian University, Tianjin 300384, China. [2] Research Center for Efficient Utilization Technology of Geothermal Energy, Tianjin Chengjian University, Tianjin 300384, China.

Received: date **Accepted: date**

Published: date

References

National Development and Reform Commission. T*he 13th Five-Year Plan for the Exploitation and Utilization of Geothermal Energy*. N.D.R.C. Publishing: Beijing, China, **2017,**Available online: http://www.ndrc.gov.cn/zcfb/zcfbtz/201702/t20170204_837203.html.(in Chinese)

China Geological Survey. *China Geothermal Energy Development Report*. Beijing, China Petrochemical Press: Beijing, China, **2018;** pp.5-10. (in Chinese)

Richard A. Beier. Transient Heat Transfer in a U-tube Borehole Heat Exchanger. *Applied Thermal Engineering* **2014**, 62, 256-266.

Richard A.B.; Marvin D.S. Reference Data Sets for Vertical Borehole Ground Heat Exchanger Models and Thermal Response Test Analysis. *Geothermics* **2011**, 40, 79-85.

Angelotti A.; Alberti L. Energy Performance and Thermal Impact of a Borehole Heat Exchanger in a sandy aquifer: Influence of the groundwater velocity. *Energy Conversion and Management* **2014**, 77, 700-708.

Jinzhong Hu. An Improved Analytical Model for Vertical Borehole Ground Heat Exchanger with Multiple-Layer Substrates and Groundwater Flow. *Applied Energy* **2017**, 202, 537-549.

Choi, J.C.; Park, J. Numerical Evaluation of the Effects of Groundwater Flow on Borehole Heat Exchanger Arrays. *Renewable Energy* **2013**, 52, 230-240.

Huajun W.; Chengying Q. Thermal Performance of Borehole Heat Exchanger under Groundwater Flow: A Case Study from Baoding. *Energy and Buildings* **2009**, 41, 1368-1373.

Alessandro C.; Rajandrea S. Efficiency of Closed Loop Geothermal Heat Pumps: A Sensitivity Analysis. *Renewable Energy* **2014**, 62, 737-746.

Yanling G.; Xiaoli Z. 3D Dynamic Numerical Programming and Calculation of Vertical Buried Tube Heat Exchanger Performance of Ground-Source Heat Pumps under Coupled Heat Transfer Inside and Outside of Tube. *Energy and Buildings* **2017**, 139, 186-196.

Jozsef H.M.; Michael d.P. Optimization of Energy Extraction for Vertical Closed-Loop Geothermal Systems Considering Groundwater Flow. *Energy Conversion and Management* **2013**, 66, 1–10.

Chaofeng L.; Peter J.C. Numerical Simulation of Ground Source Heat Pump Systems Considering Unsaturated Soil Properties and Groundwater Flow *Applied Thermal Engineering* **2018**, 139, 307-316.

Min L.; Alvin C.K. Lai. Review of Analytical Models for Heat Transfer by Vertical Ground Heat Exchangers (GHEs): A Perspective of Time and Space Scales. *Applied Energy* **2015**, 151, 178–191.

Matthew G.S.; Darin W.N. A Ground Resistance for Vertical Bore Heat Exchangers with Groundwater Flow. *Energy Resources Technology-Transactions of the ASME* **2003**, 125, 183-189.

Nairen D.; Qinyun L. Heat Transfer in Ground Heat Exchangers with Groundwater Advection. *Thermal Sciences* **2004**, 43, 1203–1211.

Nelson M.G.; Peter B. Evaluating the Influence of Thermal Dispersion on Temperature Plumes from Geothermal Systems Using Analytical Solutions. *Thermal Sciences* **2011**, 50, 1223-1231.

Nelson M.G.; Philipp B. A Moving Finite Line Source Model to Simulate Borehole Heat Exchangers with Groundwater Advection. *Thermal Sciences* **2011**, 50, 2506-2513.

Luo J.; Rohn J. A Review of Ground Investigations for Ground Source Heat Pump (GSHP) Systems. *Energy and Buildings* **2016**, 117, 160-175.

Jin L.; Joachim R. Operation Characteristics and Experience of a Ground Source Heat Pump System with a Vertical Ground Heat Exchanger. *Energy* **2013**, 51, 349-357.

Wonjun C.; Ryozo O. Interpretation of Disturbed Data in Thermal Response Tests Using the Infinite Line Source Model and Numerical Parameter estimation method. *Applied Energy* **2015**, 148, 476–488.

David C.S.; Elmore A.C. The Observed Effects of Changes in Groundwater Flow on a Borehole Heat Exchanger of a Large Scale Ground Coupled Heat pump system. *Geothermics* **2018**, 74, 240-246.

Ali S.S.; Michel B. A Small-scale Experimental Apparatus to Study Heat Transfer in the Vicinity of Geothermal Boreholes. *HVAC&R Research* **2014**, 20, 819-827.

Guozhu Z.; Yimu G. Experimental Study on the Thermal Performance of Tunnel Lining GHE under Groundwater Flow. *Applied Thermal Engineering* **2016**, 106, 784-795.

Linlin Z.; Lei Z. Analyses on Soil Temperature Response to Intermittent Heat Rejection from BHEs in Soils with Groundwater Advection. *Energy and Buildings* **2015**, 107, 355–365.

Erol S.; François B. Multilayer Analytical Model for Vertical Ground Heat Exchanger with Groundwater Flow. *Geothermics* **2018**, 71, 294-305.

Martin S.; Jonathan D. Influence of Groundwater Flow on Cost Minimization of Ground Coupled Heat Pump Systems. *Geothermics* **2018**, 73, 100-110.

Junye H.; Gui L. The Hot Stack Performance of the Shallow Geothermal Heat Pump System with/without Intensification State of Groundwater Seepage in Nanjing (China). *Energy and Buildings* **2017**, 150, 558-566.

Wenke Z.; Hongxing Y. The Research on Ring-coil Heat Transfer Models of Pile Foundation Ground Heat Exchangers in the Case of Groundwater Seepage. *Energy and Buildings* **2014**, 71, 115-128.

Østergaard P. A.; Duic N. Sustainable Development Using Renewable Energy Technology. *Renewable Energy* **2019**, 146, 2430-2437.

Nouri G.; Noorollahi Y. Designing and Optimization of Solar Assisted Ground Source Heat Pump System to Supply Heating, Cooling and Hot Water Demands. *Geothermics* **2019**, 82, 212–231.

Biglarian H.; Saidi M. H. Economic and Environmental Assessment of a Solar-assisted Ground Source Heat Pump System in a Heating-dominated Climate. *Environmental Science and Technology* **2019**, 16, 3091-3098.

Liu Z.; Li Y. Performance and Feasibility Study of Hybrid Ground Source Heat Pump System Assisted with Cooling Tower for one Office Building Based on one Shanghai Case. *Energy Conversion and Management* **2018**, 173, 28-37.

Gong X.; Xia L. Investigation on the Optimal Cooling Tower Input Capacity of a Cooling Tower Assisted Ground Source Heat Pump System. *Energy and Buildings* **2018**, 174, 239-253.

Rong Ma. Dealing with the spatial synthetic heterogeneity of aquifers in the north china plain: A case study of Luancheng County in Hebei Province. Doctoral Dissertation, Chinese Academy of Geological Sciences, Beijing, China, 2012. (in Chinese)

Zaiming Zhou. Spatial Variability and its Effect Mechanism of Soil Salinity in the Low Plain Around the Bohai Sea. Doctoral Dissertation, Chinese Academy of Geological Sciences, Beijing, China, 2012. (in Chinese)

Nam Y.; Ooka R. Development of a numerical model to predict heat exchange rates for a ground-source heat pump system. Energy and Buildings, 2008.40:2133–2140.

Antonio C.; Michele D.C. Investigations on the influence of aquifers on the ground temperature in ground-source heat pump operation. Applied Energy, 2013.107: 35.

Mao X.; Prommer H. Three-dimensional Model for Multi-component Reactive Transport with Variable Density Groundwater flow. *Environmental Modelling & Software* **2006**, 21, 615-628.

648

Nomenclature

r	distance to the source /sink(m)	$\boldsymbol{\Lambda}$	tensor of thermal hydrodynamic dispersion(W·m^{-1}·K^{-1})
t	time(s)	$\boldsymbol{\delta_{ij}}$	Kronecker tensor ($i=j$, $\delta_{ij}=1$; $i\neq j$,$\delta_{ij}=0$;)
l	tube pitch of each BHE(m)	γ	compressibility coefficient
q	heat transfer rates per unit borehole depth of the BHEs (W·m^{-1})	λ	thermal conductivity (W·m^{-1}·K^{-1})
		α_L, α_T	longitudinal and transverse thermal dispersivity, respectively, of fluid (m)
H	borehole depth(m)	ρc	volumetric heat capacity (J·m^{-3}·K^{-1})
T	temperature (K)	θ	dimensionless temperature
k	permeability(m^2)	***Subscripts***	
g	gravitational acceleration	x, y	longitudinal and transverse direction, respectively
Q_ρ	flow intensity of source (sink) term of flow field (m^3· m^{-3}·s^{-1})	r	refrigerant fluid
Q_T	heat intensity of heat source (sink) (W·m^{-3})	s	soil
x, y, z	Cartesian coordinates	f	fluid
u	absolute Darcy velocity(m·s^{-1})	s0	initial state of rock soil layer
L	dimensionless distance	m	experimental system model
$\bar{E}$	the average heat transfer efficiency coefficient	i, o	pipe-in or internal, pipe-out or outer, respectively
$\bar{Q}$	actual average heat exchange quantity (J)	***Superscripts***	
$\bar{Q}'$	theoretical average heat exchange quantity (J)	cond	conduction
M	circulating flow flux of refrigerant (m^3·s^{-1})	disp	dispersion
Greek symbols			
μ	dynamic viscosity (Pa·s)		
ε	porosity		

649

650